Potential Applications of Flat-Panel Volumetric CT in Morphologic and Functional Small Animal Imaging[1]

Susanne Greschus*, Fabian Kiessling†, Matthias P. Lichy‡,§, Jens Moll†, Margareta M. Mueller¶, Rajkumar Savai#, Frank Rose#, Clemens Ruppert#, Andreas Günther#, Marcus Luecke**, Norbert E. Fusenig¶, Wolfhard Semmler† and Horst Traupe*

*Department of Neuroradiology, University Giessen, Klinikstrasse 29, Giessen 35385, Germany; Departments of †Medical Physics in Radiology, and ‡Radiology, German Cancer Research Center, INF 280, Heidelberg 69120, Germany; §Department of Diagnostic Radiology, University of Tübingen, Hoppe-Seyler-Straße, Tübingen 72076, Germany; ¶Department of Carcinogenesis and Differentiation, German Cancer Research Center, INF 280, Heidelberg 69120, Germany; Departments of #Internal Medicine, and **Neurosurgery, University Giessen, Klinikstrasse 29, Giessen 35385, Germany

Abstract

Noninvasive radiologic imaging has recently gained considerable interest in basic and preclinical research for monitoring disease progression and therapeutic efficacy. In this report, we introduce flat-panel volumetric computed tomography (fpVCT) as a powerful new tool for noninvasive imaging of different organ systems in preclinical research. The three-dimensional visualization that is achieved by isotropic high-resolution datasets is illustrated for the skeleton, chest, abdominal organs, and brain of mice. The high image quality of chest scans enables the visualization of small lung nodules in an orthotopic lung cancer model and the reliable imaging of therapy side effects such as lung fibrosis. Using contrast-enhanced scans, fpVCT displayed the vascular trees of the brain, liver, and kidney down to the subsegmental level. Functional application of fpVCT in dynamic contrast-enhanced scans of the rat brain delivered physiologically reliable data of perfusion and tissue blood volume. Beyond scanning of small animal models as demonstrated here, fpVCT provides the ability to image animals up to the size of primates.
Neoplasia (2005) **7**, 730–740

Introduction

To simulate disease progression and develop new therapies, it is desirable to scale clinical imaging modalities to small animals. Ideally, small animal imaging modalities would be minimally invasive, deliver anatomic accuracy nearly at the histologic level, and enable the use of surrogate markers such as contrast enhancement, tissue density, or perfusion [1–3]. Prior to the development of high-resolution small animal modalities, studying cancer and other diseases using animal models was limited to *ex vivo* investigations. Longitudinal examinations had to be carried out by using biopsies, or by sacrificing animals at different tumor stages; a large number of animals are therefore required for statistically significant results. A great emphasis has been placed on adapting clinical imaging systems such as magnetic resonance imaging (MRI) [3], ultrasound [4], computed tomography (CT) [5], and nuclear medicine imaging devices [6,7]. Recently, a number of instrumentation advances in these modalities render them powerful enough to monitor small animals [8], opening new opportunities in high-resolution imaging [9–11].

A new approach, flat-panel volumetric computed tomography (fpVCT), permits the acquisition of a large volume of—rather than limited—slices per rotation, with intrinsically higher resolution than is achievable with conventional CT [12]. The system under investigation provides isotropic voxels at high resolution, which facilitates three-dimensional (3D) visualization of the imaged anatomy, and slices reformatted at arbitrary orientations with consistently high resolution.

Beyond these characteristics, the system offers a large field of view (maximum, 33 cm) and shorter scanning times (2–8 seconds per rotation) than microcomputed tomography (μCT) system, which is desirable for animal imaging. Thus, functional investigations like tissue perfusion are enabled, in combination with high resolution and a large *z*-coverage of fpVCT.

To demonstrate potential applications of fpVCT technology, in this report, we present images of mouse anatomy and pathology obtained from an experimental fpVCT system. Also, images of the same mouse, obtained from both a clinical 16-slice multislice computed tomography (MSCT) at the highest resolution and the fpVCT, are compared to each

other and to the corresponding human anatomy. Finally, quantitative analysis of brain perfusion is demonstrated in the rat.

Methods

Animals and Pathologies

All experiments were approved by the governmental review committee on animal care.

The animal models used and associated scan protocols are summarized in Table 1.

Five adult nude mice were scanned by fpVCT to study their anatomy. Inhalation anesthesia was induced and maintained with a mixture of isoflurane (1.5%), N_2O (35%), and O_2 (60%) in freely breathing animals. Catheterization of the tail vein was performed as described earlier [13] with a 30-gauge needle and an attached catheter. Scans were performed both with and without contrast agent. When used, contrast medium (0.2 ml of Iomeprol 400, 400 mg/ml iodine; Bracco-Byk Gulden, Konstanz, Germany) was manually injected starting 20 seconds before the scan, with 20 seconds of injection time.

Five C57BL/6N mice with pulmonary nodules of Lewis lung carcinoma (LLC) were examined as an example of a systemic neoplasm [14]. The animals were inoculated with LLC (LLC1; ATCC, Manassas, VA) through intratracheal injection of 10^6 cells. The cells were routinely cultured in tissue culture flasks containing RPMI 1640 medium (PAN biotech GmbH, Aidenbach, Germany) supplemented with 2% fetal bovine serum (FBS; Greiner bio one, Nuertingen, Germany), penicillin (100 U/ml), and streptomycin (0.1 mg/ml; Gibco, Eggenstein, Germany), maintained at 37°C in a humidified atmosphere containing 5% CO_2 in air.

As an example of a structural disorder, five mice with lung fibrosis induced by bleomycin were investigated [15]. Following anesthesia and orotracheal intubation, C57BL/6N mice received 5 U/kg bodyweight bleomycin (Almirall Prodesfarma, Barcelona, Spain) in a total volume of 200 μl using a microsprayer device (PennCentury, Inc., Philadelphia, PA) [16].

For scanning, the animals with both pulmonary diseases were anesthetized with an intraperitoneal injection of 0.3 ml of a solution containing 0.1 ml Rompun 2% (Bayer, Leverkusen, Germany), 0.1 ml of 100 mg/ml Ketavet (Pharmacia GmbH, Erlangen, Germany), and 0.2 ml of NaCl. No intubation was performed and no contrast agent was used for scanning either lung model.

As an example of fpVCT *ex vivo* imaging capabilities, a cast of a heart and lung generated by vascular filling with Microfil (Flow Tech, Inc., Carver, MA) was demonstrated.

Brain perfusion was studied in untreated Sprague-Dawley rats. One milliliter of Iopromid 300 (Ultravist 300; Schering, AG, Berlin, Germany) was injected into the tail vein in 2 seconds. Injection was started 2 seconds after the initialization of the first rotation. Scan interval was 2 seconds and 16 repetitions were performed. The animals were scanned while freely breathing after intraperitoneal anesthesia with Rompun/Ketavet. The head was kept firm in a head holder to avoid motion artifacts.

fpVCT

The flat-panel volumetric computed tomograph used in this study was developed and constructed by General Electric Global Research (Niskayuna, NY). A standard rotating anode X-ray tube with a focal spot size of 0.7 mm (W) × 0.6 mm (L) nominal focal spot value (IEC 336/93) is mounted on a standard gantry. The collimated X-ray beam irradiates two amorphous silicon flat-panel detectors. Each detector is composed of (1024 × 1024) 200-μm square pixels and a deposited CsI scintillator. The detectors are angled slightly toward each other on the gantry rotor. The system can be run either in "single-panel" or "dual-panel" mode, providing a maximum scanning field-of-view of 13.5 cm in a single-panel mode *vs* 32 cm in a dual-panel mode. As our subjects had a maximum diameter of 3 cm, the acquisitions were done using a single flat-panel detector. A source-to-detector distance of 783 mm and a source-to-isocenter distance

Table 1. A Detailed Overview of the Studies and Models Described, along with the fpVCT Protocol Used for Each Model.

Animal Model	Strain	Number of Animals	Intravenous Contrast Medium	Anesthesia	Scanning Parameters	Reconstruction Kernel
Mouse anatomy (no pathology)	Nude mice	5	Scanned both with no contrast agent, and with 0.2 ml of Iomeprol 400	Inhalative	Soft tissue: 70 kV/200 mA, 8 seconds per rotation, after contrast medium injection	Standard for soft tissue and angiography
					Bone/lung: 120 kV/40 mA, 8 seconds per rotation, two rotations	Edge defining for the lung and bone protocol
LLC	C57BL/6N	5	None	Intraperitoneal	120 kV/40 mA, 8 seconds per rotation, one rotation	Edge defining
Lung fibrosis	C57BL/6N	5	None	Intraperitoneal	120 kV/40 mA, 8 seconds per rotation, one rotation	Edge defining
Perfusion (no pathology)	Sprague-Dawley	4	1 ml of Iopromid 300	Intraperitoneal	70 kVp/100 mA, 2 seconds per rotation, a total of 16 rotations	Standard

Table 2. Dose Measurements Using a 10-cm Ionization Chamber in 3-cm-Outside-Diameter Acrylic Phantoms, Simulating the Body of a Mouse.

Measured in 3-cm-Diameter Acrylic Cylinder, at 70 kVp/1600 mA s

Acrylic Cylinder Wall Thickness (mm)	Measurement (mGy cm)	Dose (mGy)
		$T_{exposed}$ = 5.5 cm
0 (Air)	751.4	136.6
3.65	746.0	135.6
4.5	746.8	135.8
6	745.8	135.6

Dose was measured at 70 kVp/200 mA over 8 seconds in single-panel mode. The dose is normalized to the X-ray exposure length along the z-axis (third column).

of 540 mm result in a geometric magnification factor of 1.45 at the isocenter. The subject to be imaged is placed on a patient table that is stationary during the acquisition, whereas the X-ray tube and detector rotate around the object. For a large z-coverage investigation in multiple steps, the patient table translates further into the gantry bore for each step. A maximum z-coverage of 4.2 cm per step can be obtained at rotation times between 2 and 8 seconds. To obtain both optimal image quality and maximum z-coverage, the longest rotation time is required. Therefore, in our investigations, we chose the 8-second rotation time, which permits 1000 views and 4.2 cm of z-coverage per rotation.

Data can be acquired at X-ray energies in the range of 70 to 140 kVp. Based on recent investigations [13], the X-ray source was operated at 70 kVp with an anode current of 200 mA and 8 seconds of rotation time for soft tissue and angiographic imaging. Lung investigations were performed with 120 kVp and 40 mA, again with 8 seconds per rotation. For whole-mouse imaging, two rotations were required, with a total coverage of 8.4 cm, resulting in a total acquisition time of 16 seconds. Spatial resolution of the system was measured to be 20 to 25 lp/cm (dependent on the reconstruction filter used) at 10% MTF using a 25-μm tungsten wire in air. Raw images were reconstructed using a cone beam algorithm with both standard and edge defining reconstruction filters. The voxel size used was 0.05 mm in each spatial dimension; the reconstruction matrix was 512 × 512 for the lungs and 1024 × 1024 for whole-animal imaging. Typically, a dataset of 1500 images resulted from the reconstruction of the whole mouse, or 300 images for the thorax. All data were transferred to an Advantage Workstation 4.1 (General Electric Medical Systems Europe, Buc, France) and processed with its 3D reconstruction tool (Volume Viewer, Voxtool 3.0.58c, Buc, France) or the perfusion software (CT Perfusion Functool 2.6.0, Buc, France).

For mouse anatomy studies, the animals were anesthetized, catheterized, and centered on the fpVCT gantry axis of rotation. Baseline and contrast-enhanced fpVCT scans in nude mice were performed using identical scan parameters.

Values of 70 kVp and 100 mA were used for perfusion studies. The shortest possible rotation time in our system, 2 seconds, was used for 16 rotations, for a total scanning time of 32 seconds. Investigation of the entire head was

enabled with a z-coverage per rotation of 4.2 cm. Therefore, slices of any part of the brain could be reconstructed for perfusion analysis. This analysis is based on a deconvolution algorithm to determine the cerebral blood flow (ml/100 g per minute), blood volume (ml/100 g), and mean transit time (seconds) as described by Eastwood et al. [17]. Color-coded perfusion maps were produced to visualize the perfusion values, and measurements in specified cerebral regions of interest (frontal and parietal cortices and basal ganglia) were performed in a consensus procedure by three observers (S.G., F.K., and H.T.).

X-ray Dose Measurements in fpVCT

Dose measurements were performed using a 10-cm-long, 10-ml, CTDI-type ion chamber, placed along the axis of rotation, at the isocenter. CTDI$_{Air}$ is reported as an indication of "skin dose." To estimate the "whole-body dose" of a mouse, 3-cm-diameter acrylic cylinders with various wall thicknesses were placed over the ion chamber (Table 2). The acrylic cylinders covered the entire ion chamber. The exposed length, determined by X-ray source collimation, was 5.5 cm. The data show no significant difference between these measurements and CTDI$_{Air}$. Therefore, with the spectra used, the whole-body exposure of a mouse can be estimated by the exposure in air: 137 mGy at 70 kVp/1600 mA s and 96 mGy at 120 kVp/320 mA s (Table 3). For the perfusion exam, a 70-kVp/3200 mA s technique was used, so the dose was 274 mGy.

For reference purposes, although not relevant to mouse scans, in the center of a 16-cm-diameter acrylic CTDI head phantom, CTDI$_{100}$ was measured to be 73.3 mGy (70 kVp/1600 mA s) and 64.7 mGy (120 kVp/320 mA s) (Table 4).

MSCT

A 16-slice CT system (Aquilion 16; Toshiba, Neuss, Germany) was used for exemplary comparison between MSCT and fpVCT imaging capability. To match the MSCT and fpVCT scan parameters as closely as possible, an axial imaging mode with a minimal slice thickness of 0.5 mm was chosen, the rotation time was set to 1500 milliseconds per rotation, and the field-of-view was reduced to a minimum of 18 cm. The lowest possible voltage of 80 kVp was used with a tube current of 200 mA. Contrast medium application was the same as with fpVCT examinations.

Table 3. Dose Measurements Using a 10-cm Ionization Chamber in Air.

Measured in Air

kVp/mA s	Measurement (mGy cm)	Dose (mGy)
		$T_{exposed}$ = 5.5 cm
70/1600	751.4	136.6
120/320	525.6	95.6

Dose was measured at 70 kVp/200 mA and 120 kVp/40 mA over 8 seconds in single-panel mode.
The dose is normalized to the X-ray exposure length along the z-axis (third column).

Table 4. Dose Measurements Using a 10-cm Ionization Chamber in a 16-cm-Diameter Acrylic CTDI Head Phantom (Clinical Standard).

Measured in 16-cm-Diameter CTDI Head Phantom		
kVp/mA s	Measurement (mGy cm)	Dose (mGy)
		$T_{exposed}$ = 5.5 cm
70/1600	403.2	73.3
120/320	356.0	64.7

Here measurements were performed in dual-panel mode, deviating from the other protocols, because this mode would be used for measurements of larger subjects.

Dose was measured at 70 kVp/200 mA and 120 kVp/40 mA over 8 seconds. The dose is normalized to the X-ray exposure length along the z-axis (third column).

Histology

Dedicated organs (brain, kidneys, liver, heart, lung, and spleen) were removed from the animals for histology. All organs were fixed in 4% paraformaldehyde overnight at 4°C and embedded in paraffin. They were cut in 5-μm-thick slices and stained with hematoxylin and eosin (H&E). Tissue sections were viewed using an Olympus AX-70 microscope (Olympus Corp., Hamburg, Germany). Images were captured with an analySIS color view 12 digital camera (Soft Imaging System, Muenster, Germany) and morphometric analyses were performed at ×100 magnification using the analytic SIS (Soft Imaging System) software. The SIS software was also used to perform distance measurements on

microscopic images. The inner diameters of the cerebral and renal arteries and veins were determined. The ventricular system of the brain was measured using the largest and shortest diameters of the structures delineated by the parenchyma.

Fibrosis was proven with H&E and trichrome staining in histology, quantification of collagen content by hydroxyproline assay, and functional compliance measurements.

Results

Animal Imaging

Contrast medium application and tomography were well tolerated by the animals without any apparent clinical side effects during a 1-week observation time. We did not observe any changes in behavior, signs of distress, or stroke, nor did we have a fatal complication following the scans. Measurement of body weight was constant; therefore, severe renal function was not indicated.

Bone

The large difference in attenuation between bone and soft tissue was captured by fpVCT and therefore enabled the selective 3D visualization of the skeleton (Figure 1). At the limbs, the adjacent joints including the intra-articular clefts down to the single tarsal and metatarsal bones were well defined. In the spine, the spinal canal with the outlets
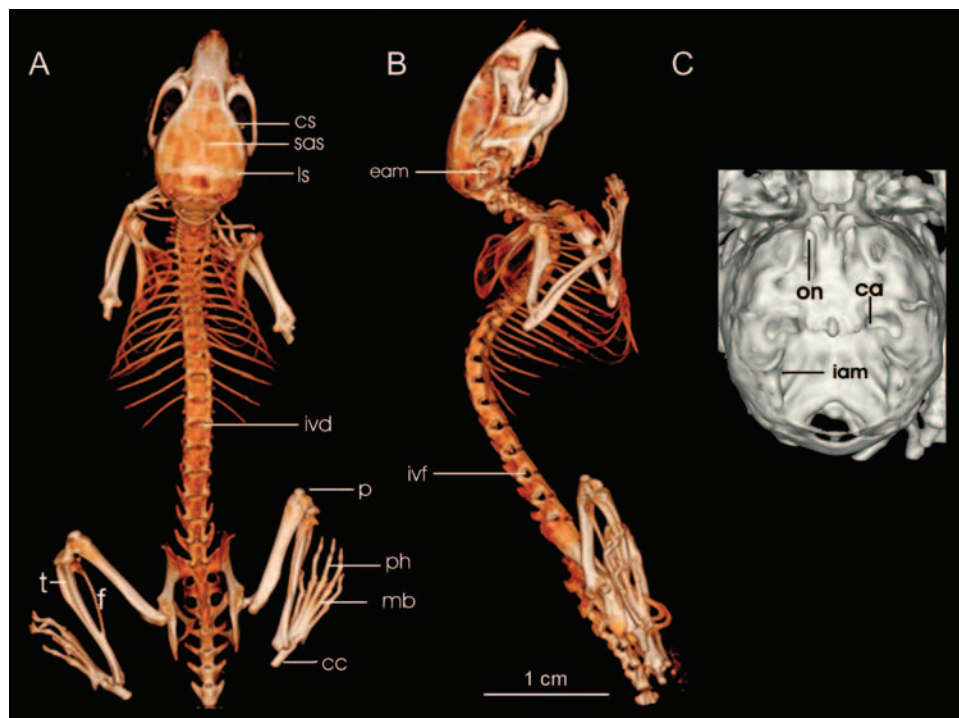

Figure 1. *3D imaging of the skeleton with a volumetric rendering technique based on thresholding of the fpVCT dataset (A and B) is shown. Excellent image quality of the spine, with differentiation of every single vertebra, intervertebral discs (ivd), and intervertebral foramina (ivf), is achieved in nonenhanced scans. Small elements like calcaneus (cc), metatarsal bones (mb), and phalanges (ph), as well as the joints of the long bones (t = tibia, f = fibula, p = patella), such as knee joints and femoral articulations, can be studied in detail. High resolution becomes evident in a detailed depiction of the skull with differentiation of the coronal (cs), sagittal (sas), and lambdoid suture (ls), or the external acoustic meatus (eam). On the magnification of the cranial bone (C), even the large foramina, such as the inlet for the carotid (ca) and the optic nerve (on) or the internal acoustic meatus (iam), are clearly visualized. Bar = 1 cm.*

for spinal nerves through the intervertebral foramina can be studied. At lumbar vertebra corticalis and spongiosa, the attached intervertebral and costovertebral joints were clearly delineated (Figures 1, *A* and *B*, and 2). At the skull base with its small foramina, the inlet of the carotid artery and optic nerve as well as the internal acoustic meatus can be identified (Figure 1*C*). In comparison with MSCT, fpVCT shows a higher anatomic detail of bone structures in the small animal (e.g., the corticalis of the bones and vertebrae appear to be blurred on the MSCT but they are sharply displayed in the fpVCT images). In addition, the intervertebral clefts are clearly delineated only in the fpVCT images (Figure 2).

Thorax

Imaging the lung architecture does not require contrast medium application. Although the acquisition time is much longer than the time of one breath of a normal active mouse (respiration frequency ~ 160 min^{-1} [18], or ~ 21 breaths during one scan), no visible motion artifacts were observed and the lung structure was clearly displayed. Because the scan times cannot realistically be reduced to the rest phase of one respiration cycle, a future option for further improvement of image quality could be retrospective respiratory gating. Other alternatives are intubation and forced breath-hold during the scan, although these are highly invasive procedures, which might not completely eliminate lung motion. Visualization of ventilated lung parenchyma, from the bronchi down to the third trunk generation and subsegmental pulmonary arteries, was successfully achieved (Figure 3, *A–D*). In some cases, even lung septa in healthy animals could be identified, although they were most frequently seen in animals with lung fibrosis. The high isotropic resolution facilitated the 3D visualization, permitting segmentation of the bronchial system, alveolar tissue, or the vasculature.

Besides normal lung anatomy, fpVCT can detect pulmonary pathologies, which is exemplarily shown for nodules of a LLC (Figure 3*E*).
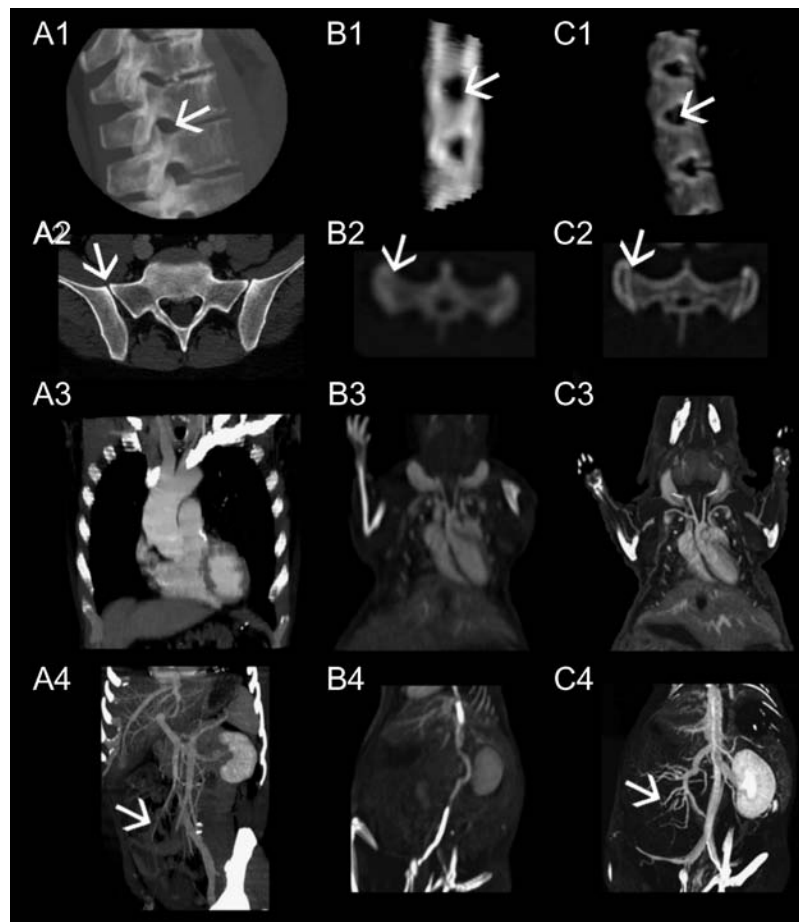

Figure 2. *High-resolution images from a 16-slice MSCT (Aquilion 16; Toshiba) of a human thorax and spine (A) are compared to scans of a mouse with the same system (B) and with the fpVCT (C). It is well demonstrated that the spine is shown in great detail in $A_{1,2}$ and $C_{1,2}$, although there is a 20-fold difference in size between the species, but blurred images of the mouse spine in $B_{1,2}$ do not permit the investigation of bone structure and density (arrow pointing on the intervertebral foramen in $A_1–C_1$). The latter gives only a vague impression of the first sacral vertebra with the sacro-iliacal junction (B_2), whereas a detailed view is obtained with mouse fpVCT images and human MSCT images (arrows in $A_2–C_2$). With contrast medium application, the cardiovascular system is displayed in detail, with sharp delineation of small vessels with fpVCT (C_3). Comparable resolution is gained in MSCT of the human scan (A_3), but this scanner cannot compete with fpVCT concerning the resolution required for the scan of the mouse (B_3). The same is true for visualization of the abdomen ($A_4–C_4$). Here, the lienal vein and its confluence with the mesenteric vein into the portal vein, as well as the inflow of the small intestinal veins to the mesenteric vein, are only visible in the mouse with fpVCT and in the human with MSCT (arrows in A_4 and C_4).*
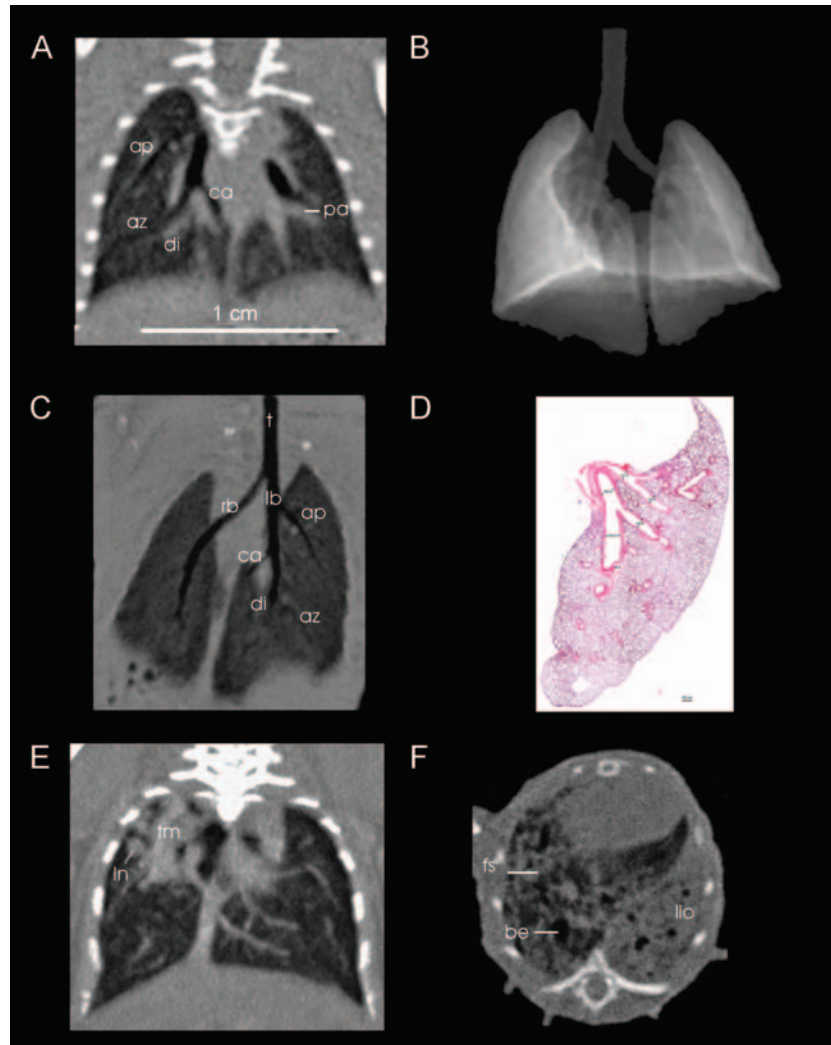
Figure 3. *Different aspects of thoracic imaging of mice are demonstrated. On a reformatted image in coronal view (A), the effect of isotropic resolution is impressively demonstrated, as there is no deficit in spatial resolution or image distortion in the z-direction. Even in this baseline scan, the pulmonary arteries (pa) are well delineated. After segmentation of the lungs from the thorax (threshold-based surface rendering in B), the airways are visualized in three dimensions (minimum intensity projection image C, coronal view) and can be followed from the trachea (t) to the main bronchi (rb = right bronchus, lb = left bronchus), with the segmental bronchi supplying the apical (ap), cardiac (ca), diaphragmatic (di), and azygous (az) lobes on the right side (left side in the image) down to the subsegmental bronchi. This fpVCT image can be compared to a histologic slice of the left lung (D, coronal orientation). The left bronchus and its branches were measured to be 1.81, 1.26, 2.04, and 1.21 mm in diameter. All structures are clearly delineated in fpVCT images. Orthotopic LLC model (E): the nodules (ln) and a confluent tumor mass (tm) are clearly localized in the upper part of the right lung (left in the image). Lung fibrosis model (F): the typical manifestation of pulmonary fibrosis is displayed in a mouse treated with bleomycin. The lung structure shows bronchiectasis (be), fibrotic threads (fs), and fibrotic consolidation of the left lobe (llo). Bar = 1 cm.*

As a second example, bleomycin-induced pulmonary fibrosis at 14 days after bleomycin application is shown (Figure 3F). At this time, structural abnormality—starting with ground glass opacity and septal thickening, then progressing to severe consolidation of the tissue, fibrotic strands, and secondary dilation of the bronchial system (bronchiectasis)—could be visualized clearly. The animals with severe lung changes showed clinical symptoms like kyphosis, reduced activity, and tachypnea. However, early indications of fibrosis could be identified in scans of clinically asymptomatic animals.

After contrast medium injection, angiographies of the mouse thorax were generated (Figure 4, *A–C*). Images of cardiac structures with differentiation of the right and left ventricles and atria as well as ingoing veins and outgoing arteries were achieved in 3D reconstructions. Although information obtained concerning the coronary arteries in the beating heart was limited, localization of these vessels in *ex vivo* images obtained from a cast of the lung and heart was possible (Figure 4*D*).

Abdomen

With fpVCT, parenchymal organs could be characterized by the pattern of contrast medium uptake in mice, in detail comparable to human images acquired with clinical MSCT. In our examinations, liver segments were assigned using the liver veins as landmarks, which formed the segment borders and were clearly visible in all contrast-enhanced fpVCT scans. The portal vein could be followed to the entrance into
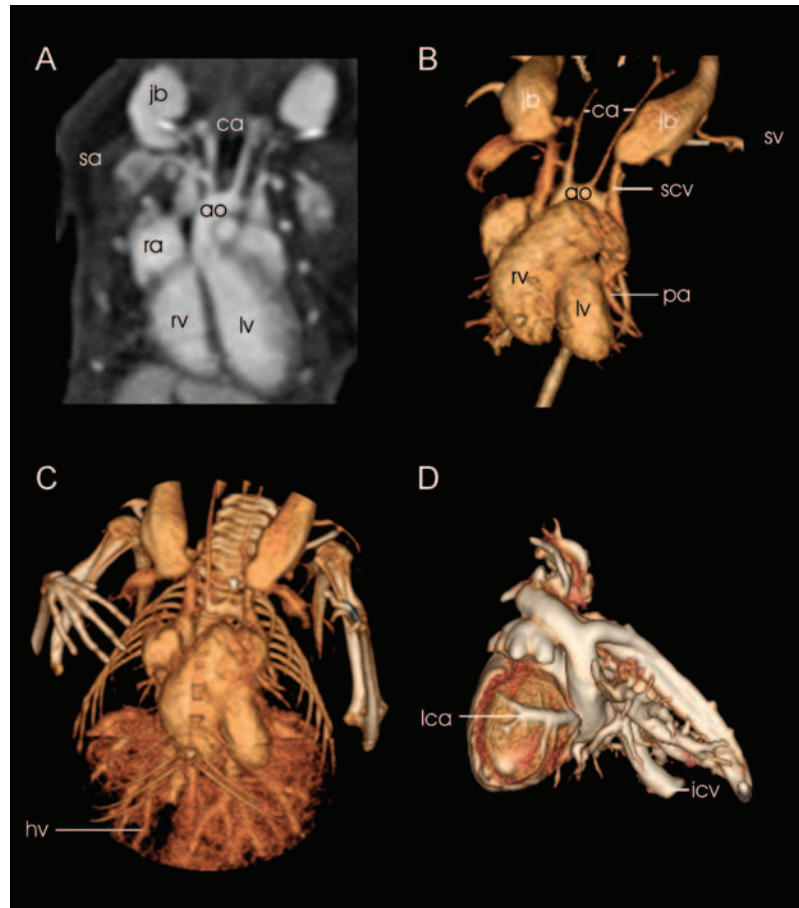
Figure 4. *These datasets are acquired after application of contrast medium. Sagittal reformatting (A) shows the contrast-filled right atrium (ra), left ventricle (lv), and right ventricle (rv) of the heart. The aortic arch (ao) with outlet of the carotid arteries (ca) and subclavian arteries (sa) can clearly be delineated in the raw images. Excellent vessel contrast determines the quality of 3D segmentation of the cardiopulmonary system (B and C) where the pulmonary arteries (pa) are clearly rendered. Together with the prominent jugular bulbs (jb), the subclavian veins (sv), the inferior vena cava (icv), and the pairwise developed superior vena cava (svc), the visibility of arterial and venous vessel contrasts is demonstrated. The vascular tree of the liver is well differentiated, revealing the hepatic veins (hv) and the portal vein (not shown) after its formation by the intestinal, gastric, and splenic veins. In a cast of the heart and adjacent vessels (D), also the coronary arteries (lca = left coronary artery) can also be visualized in a 3D segmentation.*

the hepatic portal after conjunction with the intestinal and splenic veins (Figure 2, C_3).

As in other mammals, iodinated contrast medium carries the risk of renal toxicity when injected in mice. The contrast medium dose was adapted to the body weight, and the elimination of the substance by the kidneys through the urogenital tract could be followed. The three phases of kidney perfusion could be observed by repeated scanning. Images acquired during the arterial phase displayed the renal artery and its branches up to the subsegmental vessels. Their inner diameter was measured with histology to be an average of 46.2 μm. Scanning during the venous phase allowed the differentiation of the cortex and the medulla; in a third phase, the contrast medium elimination into the pyelon, ureter, and bladder could be visualized (Figure 5). In further examples of animal anatomic delineation, the adrenal glands were clearly shown above the kidneys, and the ovaries were visible below. Neither organ showed a detailed parenchymal differentiation, although, in both cases, volumetry of the whole organ was possible.

The entire aorta could consistently be tracked from the thorax to the abdominal cavity, down to its branching into the two iliacal arteries. In the arterial phase, the outlet of the renal arteries and even the adrenal arteries were identified and assigned in 3D renderings.

Brain Anatomy

In fpVCT angiographic images of nude mice, the brain-supplying arteries were tracked from their origin in the aortic arch up to their entry into the skull base. Intracerebral identification of the internal carotid artery and the anterior, posterior, and middle cerebral arteries was achieved. In addition, large veins like the superior sagittal sinus were clearly visualized (Figure 6). Diameters of the basal arteries were determined by comparison to histologic images and ranged from 42 to 55 μm with an average of 47 μm (*n* = 5). Parts of the ventricular system could be identified in nonenhanced fpVCT images. Delineation of the third ventricle, which was presented as a small slit between the thalami, was improved by bright enhancement of the choroid plexus
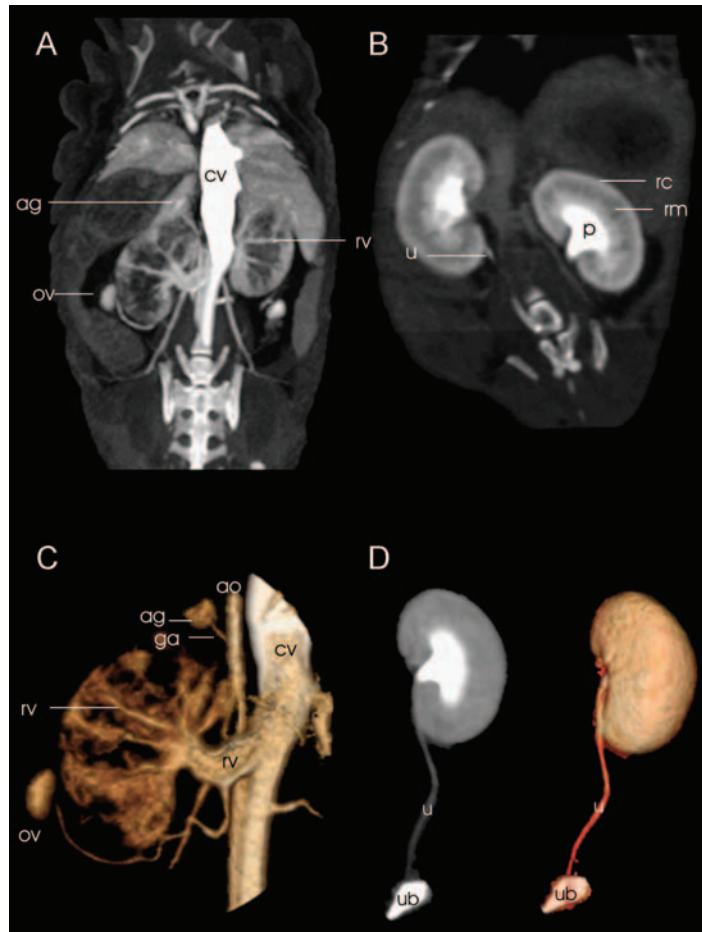
Figure 5. *Ten seconds after contrast medium injection (A), the inferior vena cava (cv) shows a prominent enhancement in this maximum intensity projection (MIP) displayed in a coronal view. Renal vasculature can be followed from the renal artery and vein (rv) to the interlobar artery and vein, down to the interlobular level of the vessels. Eight minutes later, another scan documents the elimination of the contrast medium into the pyelon (B). A clear cortico-medullar (cortex = rc, medulla = rm) differentiation is evident. Now the parenchyma is diffusely enhanced, whereas the intrarenal vessels are not distinguishable anymore. Both phases (A and B) can be used for 3D segmentation. In panel C, a 3D segmentation (volume rendering) of the first phase, the renal vasculature is tracked from its outlet. In this view, feeding of the adrenal gland (ag) by an artery from the aorta (suprarenal artery = ga) is demonstrated. Another vessel, the ovarian vein, which drains the ovary (ov), can be followed to the renal vein (rv). The renal pyelon (p; panel B) is contrast-filled after 8 minutes. The contrast flow can be followed through the ureters (u) down to the urinary bladder (ub) after 3D segmentation with an MIP (D, left) or surface rendering (D, right), observing the excretion of the contrast medium in the third phase of contrast elimination.*

after contrast medium application. Also, the fourth ventricle, with a maximal transversal dimension of 330 μm as determined by histology, was visualized in fpVCT, showing its typical rhomboid shape.

Brain Perfusion

Due to smaller dimensions of mice, the display of mouse anatomy was more challenging and therefore was chosen for the previous anatomic examples. However, rats were used for perfusion studies because these were the most frequently used animals for stroke experiments.

Blood perfusion in different areas of the rat brain was analyzed quantitatively. Three parameters—cerebral blood flow (CBF), mean transit time (MTT), and cerebral blood volume (CBV)—were calculated and their distribution was displayed in color-coded maps (Figure 7). In this example, mean CBV was determined as 3.7 ± 0.4 ml/100 g, CBF was 97.3 ± 10.2 ml/100 g per minute, and the mean value for MTT was 2.8 ± 0.5 seconds, calculated in the frontal

and parietal cortices and in the basal ganglia. These results match well with previously reported data from different modalities and animal models [19,20]. In the first reference, measurements were based on synchrotron radiation quantitative computed tomography. Mean CBV and CBF in the parietal cortex were 2.1 ± 0.38 ml/100 g and 129 ± 18 ml/100 g per minute *vs* 1.92 ± 0.32 ml/100 g and 125 ± 17 ml/100 g per minute in the caudate−putamen. In this study, MTT was not determined. MTT values measured in beagles [20] with CT were determined in 2.4 to 3.0 seconds, depending on the location of the measurements.

Comparing fpVCT with MSCT

Although, to some extent, MSCT allows the imaging of anatomic structures in small animals, Figure 2 demonstrates the considerable difference between resolutions in fpVCT and MSCT. fpVCT images offer a sharply delineated view of the circulation after injection of contrast medium, whereas only a blurred view is achieved in MSCT. The latter specifically
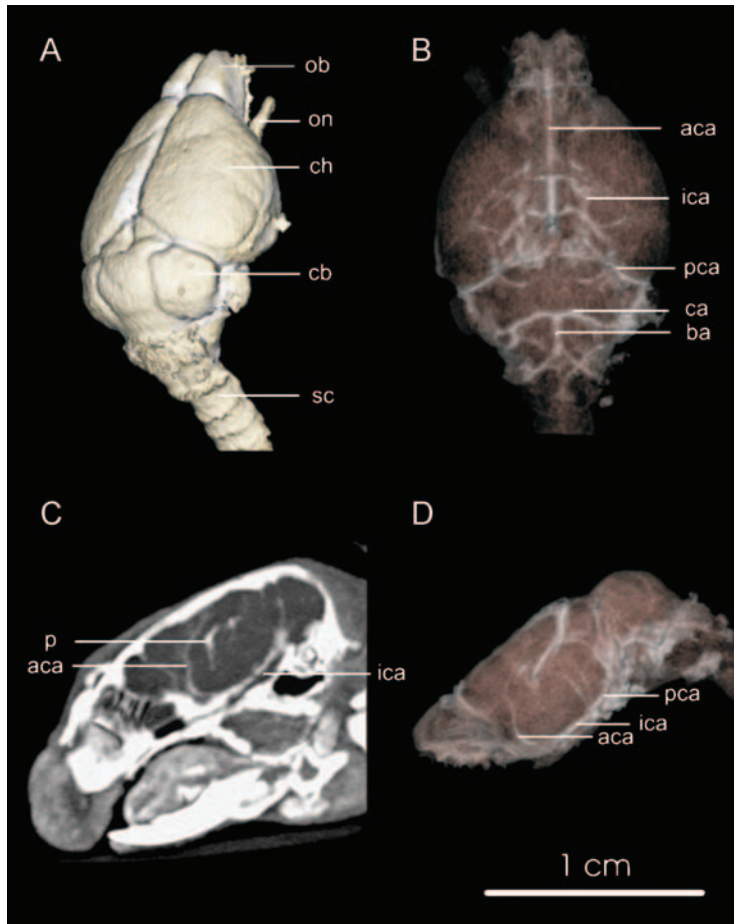
Figure 6. *Cerebral imaging of the mouse. In panel A, the cerebral surface with the olfactory lobe (ol), the cerebral hemispheres (ch), the cerebellum (cb) with the cerebellar hemispheres (cbh), as well as the optical nerve (on), resembling a protruded part of the cerebrum and the spinal chord (sc), are rendered. Techniques for visualization of the vessels, like volume rendering (B and D) or MIP (C), enable angiographic images, assuming use of contrast agent. The main basal cerebral arteries are labeled (aca = anterior cerebral artery, pca = posterior cerebral artery, mca = middle cerebral artery, ca = cerebellar artery), which can be tracked from their origin from the basilar artery (ba) and from the internal carotid artery (ica). Parts of the venous systems can be followed, indicated by veins debouching into the superior sagittal sinus (sss). Contrast enhancement of the choroid plexus (p) denotes the location of the cerebral ventricles. Bar = 1 cm.*

fails in the visualization of the small arteries (e.g., the circulation of the brain or kidneys). Finally, a 3D display or segmentation of the anatomy in fpVCT, enabled by isotropic resolution of fpVCT, provides additional topographic orientations and yields more accurate delineations of anatomic fine structures than can be achieved with MSCT. Comparison of fpVCT
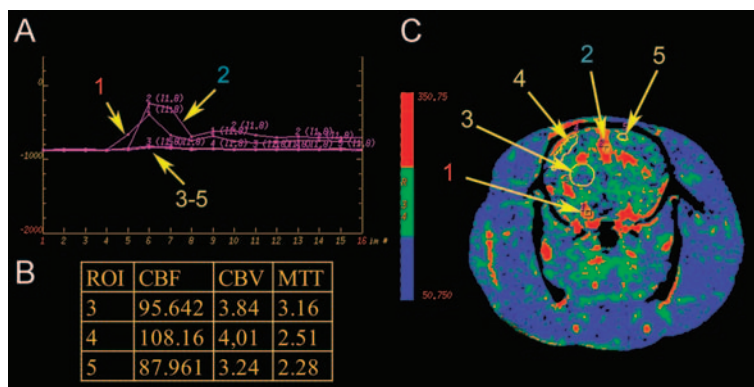

Figure 7. *Perfusion images of the rat brain were obtained after intravenous application of 1 ml of Iomeprol and scanning performed in cine mode with 2 seconds of rotation time over 32 seconds. Panel A shows the attenuation curves of the artery (1), vein (2), and three regions of interest. Region (3) covers parts of the basal ganglia; region (4) is located in the right parietal cortex; and region (5) is located in the left frontal cortex. The corresponding perfusion map for the cerebral blood flow is given in panel C and measured values for CBF (ml/100 g per minute), CBV (ml/100 g), and MTT (seconds) are given in the table (B).*

images of a mouse with clinical MSCT images of a human clearly demonstrates a similar image quality. This confirms that the objective to scale imaging capability from humans to small animals is realized in many aspects by fpVCT.

Discussion

In this study, the morphologic appearance of mouse anatomy is shown using an experimental computed tomograph equipped with flat-panel detectors. The details of the mouse skeleton and vascular systems are resolved with fpVCT. Comparison of the smallest visualized structures, like renal arteries and cerebral ventricles, with histologic images gives an estimate of the resolution capabilities and limitations of the system. Images of the identical mouse, obtained with the fpVCT, are compared with those from a clinical 16-slice CT scanner, and also compared with images of the corresponding anatomy of humans, obtained with the same clinical scanner. Furthermore, preliminary data of successful perfusion scanning of a rat brain are presented.

The detailed visualization of the mouse skeleton, with clear contours of smaller bones and vertebrae, suggests that high-resolution fpVCT can be effectively used for morphologic animal phenotyping [21] and thus supplementation of molecular imaging modalities for gene detection [22,23]. The differentiation between the cortex and the spongiosa provided by fpVCT is a prerequisite for the detection of osseous lesions like metastases [24]. For fine structure analysis, such as the evaluation of early osteoporotic disease and the analysis of trabecular architecture, the resolution might not be sufficient and may remain the domain of μCT [25].

Long-term studies of metastasizing tumor models and longitudinal observations of orthotopic lung tumor models [26,26] require high-resolution lung imaging capability. In this context, fpVCT is valuable because it can detect small pulmonary nodules and structural changes such as fibrosis, which might occur as a side effect from therapies. Short scanning times allowed noninvasive anesthesia for follow-up studies.

CT perfusion (CTP) is a well-established and clinically applied method in acute stroke, stroke follow-up studies, and differentiation of brain tumors. The method quantifies regional CBV and MTT, and allows the calculation of regional CBF. Until now, one of the biggest drawbacks of CTP is incomplete volume coverage of the organ of interest. fpVCT allows blood flow measurements in whole organs of small animals (e.g., the brain or the heart). Compared to commonly used experimental techniques like autoradiography ormicrosphere techniques, CTP in thin slices allows perfusion studies covering the whole brain, and therefore is the first experimental method that permits noninvasive long-term studies of whole-brain perfusion. The preliminary data shown in this study indicate that fpVCT data on cerebral blood flow parameters in rats are comparable to those known from the literature. Quantitative analysis of perfusion data is limited by the 2-second minimum rotation time with this experimental fpVCT system. Depending on the contrast medium dose, longer rotation times of up to 4 seconds produced reasonable accuracy in humans, as

recently described by Wintermark et al. [27]. However, considering the short circulation time of small animals, the minimum rotation time of this experimental fpVCT scanner may have to be adapted to animal models. We have demonstrated that the temporal resolution in dynamic scans is sufficient to provide reliable data in the rat brain vascularization, although this has to be evaluated in larger studies and the accuracy may benefit from a slightly faster rotation time (approximately 0.5 seconds). Then fpVCT could become an important tool for stroke research, and also for perfusion analysis of other organs as well as tumors.

Dedicated high-resolution animal μCT systems are commercially available. In contrast to μCT, where scanning at a resolution of 50 μm or less demands scanning times of several minutes, the acquisition time with fpVCT is, at most, 8 seconds; therefore, the susceptibility to motion artifacts is dramatically reduced. In addition and in contrast to μCT, *in vivo* contrast medium application is effective due to short scanning time, which does not exceed the animal's vascular elimination time. The combination of short scan times and use of contrast agent permits functional imaging (e.g., perfusion studies as described above, which cannot be performed with μCT). Even the use of some blood-pool contrast agents may not be sufficient to provide a reliable contrast because the iodine concentrations are much lower than in conventional contrast media (300–400 mg/ml for conventional contrast agents *versus* approximately 50 mg/ml for currently available blood-pool agents). However, only high concentration provides sufficient contrast to clearly delineate not only the small primary vessels in small animals, but also tumor neovasculature. Angiographic images can therefore be generated. In prior work, it has been shown that with the use of contrast medium, even extremely small vessels inside tumors can be visualized, permitting use of the system for imaging angiogenesis [13] and therefore offering an option in monitoring antiangiogenic approaches in tumor therapy [28,29]. A further advantage of fpVCT over μCT is the reduction of radiation dose. Risk of radiation dose–induced biologic impact with μCT has been described [30–32]. Compared to the dose for *in vivo* mouse scans reported in those studies, in the range of 210 to 380 mGy, fpVCT dose is substantially lower (in the range of 96–137 mGy, as reported above). Even in long-term studies on skeletal development, with 11 to 14 scans over the course of up to 51 days, the dose was below critical ranges on biologic integrity [33].

Conclusion

fpVCT provides a high spatial resolution imaging of rodents, which is superior to clinical MSCT scanners but currently lower than possible with μCT. However, as compared with μCT, fpVCT enables shorter scan times, and is therefore less invasive with respect to radiation dose and anesthesia. fpVCT enables perfusion imaging at sufficiently high resolution to be applicable to small animals. fpVCT also enables long-term longitudinal studies, which, compared to μCT, employ minimally invasive anesthesia and breath control protocols, and substantially lower radiation dose. In summary, for small animal

imaging, fpVCT fills a gap between clinical MSCT and preclinical μCT systems, and is highly suited for studying orthotopic and metastasizing tumor models, as well as for diseases requiring short scan times like stroke and lung investigations.

References

[1] Hirsch J (2003). Imaging and biological function in health and disease. *J Clin Invest* **111,** 1440–1443.

[2] Weissleder R and Mahmood U (2001). Molecular imaging. *Radiology* **219,** 316–333.

[3] Kiessling F, Heilmann M, Vosseler S, Lichy M, Krix M, Fink C, Kiessling I, Steinbauer H, Schad L, Fusenig NE, et al. (2003). Dynamic T1-weighted monitoring of vascularization in human carcinoma heterotransplants by magnetic resonance imaging. *International Journal of Cancer* **104,** 798.

[4] Krix M, Kiessling F, Vosseler S, Farhan N, Mueller MM, Bohlen P, Fusenig NE, and Delorme S (2003). Sensitive noninvasive monitoring of tumor perfusion during antiangiogenic therapy by intermittent bolus–contrast power Doppler sonography. *Cancer Res* **63,** 8264–8270.

[5] Liao ZX, Travis EL, and Tucker SL (1995). Damage and morbidity from pneumonitis after irradiation of partial volumes of mouse lung. *Int J Radiat Oncol Biol Phys* **32,** 1359–1370.

[6] Weissleder R (1999). Molecular imaging: exploring the next frontier. *Radiology* **212,** 609–614.

[7] Kondo M, Asai T, Katanasaka Y, Sadzuka Y, Tsukada H, Ogino K, Taki T, Baba K, and Oku N (2004). Anti-neovascular therapy by liposomal drug targeted to membrane type-1 matrix metalloproteinase. *Int J Cancer* **108,** 301–306.

[8] Weissleder R (2002). Scaling down imaging: molecular mapping of cancer in mice. *Nat Rev Cancer* **2,** 11–18.

[9] Lewis JS, Achilefu S, Garbow JR, Laforest R, and Welch MJ (2002). Small animal imaging. current technology and perspectives for oncological imaging. *Eur J Cancer* **38,** 2173–2188.

[10] Michalowski J (2001). Imaging facilities focus on small animal research. *J Natl Cancer Inst* **93,** 1773–1774.

[11] Allport JR and Weissleder R (2001). *In vivo* imaging of gene and cell therapies. *Exp Hematol* **29,** 1237–1246.

[12] Kalender WA (2003). The use of flat-panel detectors for CT imaging. *Radiology* **43,** 379–387.

[13] Kiessling F, Greschus S, Lichy MP, Bock M, Fink C, Vosseler S, Moll J, Mueller MM, Fusenig NE, Traupe H, et al. (2004). Volumetric computed tomography (VCT): a new technology for noninvasive, high-resolution monitoring of tumor angiogenesis. *Nat Med* **10,** 1133–1138.

[14] Li LM, Shin DM, and Fidler IJ (1990). Intrabronchial implantation of the Lewis lung tumor cell does not favor tumorigenicity and metastasis. *Invasion Metastasis* **10,** 129–141.

[15] Chapman HA (2004). Disorders of lung matrix remodeling. *J Clin Invest* **113,** 148–157.

[16] Schmidt R, Ruppert C, Markart P, Lubke N, Ermert L, Weissmann N, Breithecker A, Ermert M, Seeger W, and Gunther A (2004). Changes in pulmonary surfactant function and composition in bleomycin-induced pneumonitis and fibrosis. *Toxicol Appl Pharmacol* **195,** 218–231.

[17] Eastwood JD, Provenzale JM, Hurwitz LM, and Lee TY (2001). Practical injection-rate CT perfusion imaging: deconvolution-derived hemodynamics in a case of stroke. *Neuroradiology* **43,** 223–226.

[18] Fox JG and Cohen BJ (1984). *Laboratory Animal Medicine.* Harcourt Publishers, Ltd., London, GB.

[19] Adam JF, Elleaume H, Le Duc G, Corde S, Charvet AM, Tropres I, Le Bas JF, and Esteve F (2003). Absolute cerebral blood volume and blood flow measurements based on synchrotron radiation quantitative computed tomography. *J Cereb Blood Flow Metab* **23,** 499–512.

[20] Nabavi DG, Cenic A, Craen RA, Gelb AW, Bennett JD, Kozak R, and Lee TY (1999). CT assessment of cerebral perfusion: experimental validation and initial clinical experience. *Radiology* **213,** 141–149.

[21] Hill NL, Laib A, and Duncan MK (2002). Mutation of the *ectodysplasin-A* gene results in bone defects in mice. *J Comp Pathol* **126,** 220–225.

[22] Jacobs A, Dubrovin M, Hewett J, Sena-Esteves M, Tan CW, Slack M, Sadelain M, Breakefield XO, and Tjuvajev JG (1999). Functional co-expression of HSV-1 thymidine kinase and green fluorescent protein: implications for noninvasive imaging of transgene expression. *Neoplasia* **1,** 154–161.

[23] Gambhir SS, Herschman HR, Cherry SR, Barrio JR, Satyamurthy N, Toyokuni T, Phelps ME, Larson SM, Balatoni J, Finn R, et al. (2000). Imaging transgene expression with radionuclide imaging technologies. *Neoplasia* **2,** 118–138.

[24] Neudert M, Fischer C, Krempien B, Bauss F, and Seibel MJ (2003). Site-specific human breast cancer (MDA-MB-231) metastases in nude rats: model characterisation and *in vivo* effects of ibandronate on tumour growth. *Int J Cancer* **107,** 468–477.

[25] Borah B, Gross GJ, Dufresne TE, Smith TS, Cockman MD, Chmielewski PA, Lundy MW, Hartke JR, and Sod EW (2001). Three-dimensional microimaging (MRmicroI and microCT), finite element modeling, and rapid prototyping provide unique insights into bone architecture in osteoporosis. *Anat Rec* **265,** 101–110.

[26] Kennel SJ, Davis IA, Branning J, Pan H, Kabalka GW, and Paulus MJ (2000). High resolution computed tomography and MRI for monitoring lung tumor growth in mice undergoing radioimmunotherapy: correlation with histology. *Med Phys* **27,** 1101–1107.

[27] Wintermark M, Smith WS, Ko NU, Quist M, Schnyder P, and Dillon WP (2004). Dynamic perfusion CT: optimizing the temporal resolution and contrast volume for calculation of perfusion CT parameters in stroke patients. *AJNR Am J Neuroradiol* **25,** 720–729.

[28] Kerbel RS (2004). Antiangiogenic drugs and current strategies for the treatment of lung cancer. *Semin Oncol* **31,** 54–60.

[29] Khan MK, Miller MW, Taylor J, Gill NK, Dick RD, Van Golen K, Brewer GJ, and Merajver SD (2002). Radiotherapy and antiangiogenic TM in lung cancer. *Neoplasia* **4,** 164–170.

[30] Boone JM, Velazquez O, and Cherry SR (2004). Small-animal X-ray dose from micro-CT. *Mol Imaging* **3,** 149–158.

[31] Paulus MJ, Gleason SS, Kennel SJ, Hunsicker PR, and Johnson DK (2000). High resolution X-ray computed tomography: an emerging tool for small animal cancer research. *Neoplasia* **2,** 62–70.

[32] Ford NL, Thornton MM, and Holdsworth DW (2003). Fundamental image quality limits for microcomputed tomography in small animals. *Med Phys* **30,** 2869–2877.

[33] Obert M, Ahlemeyer B, Baumgart-Vogt E, and Traupe H (2005). Flat-panel volumetric computed tomography—a new method for visualizing fine bone detail in living mice. *J Comput Assist Tomogr* (in press).